Maritime Moving Target Indication Using Passive GNSS-based Bistatic Radar

Ma, H.; Antoniou, M.; Pastina, D.; Santi, F.; Pieralice, F.; Bucciarelli, M.; Cherniakov, M.

DOI:
10.1109/TAES.2017.2739900

License:
Other (please specify with Rights Statement)

Document Version
Peer reviewed version

Citation for published version (Harvard):
Ma, H, Antoniou, M, Pastina, D, Santi, F, Pieralice, F, Bucciarelli, M & Cherniakov, M 2017, 'Maritime Moving Target Indication Using Passive GNSS-based Bistatic Radar', *IEEE Transactions on Aerospace and Electronic Systems*, vol. PP, no. 99. https://doi.org/10.1109/TAES.2017.2739900

Maritime Moving Target Indication Using Passive GNSS-based Bistatic Radar

H. Ma[1,2], M. Antoniou[1], D. Pastina[3], F. Santi[3], F. Pieralice[3], M. Bucciarelli[4], M. Cherniakov[1]

[1]School of Electronic, Electrical and System Engineering, University of Birmingham, Birmingham B15 2TT, U.K.

[2]National Laboratory of Radar Signal Processing, Xidian University, Xi'an, 710071, China

[3]Department of Information Engineering, Electronics and Telecommunications, University of Rome "La Sapienza", 00184 Rome, Italy

[4]Sympas S.r.l., viale Giulio Cesare 71 – 00192 Rome

***Abstract*—This paper is a first introduction to the concept of using Global Navigation Satellite Systems (GNSS) as illuminators of opportunity in a passive bistatic real-time radar system for maritime target indication applications. An overview of the system concept and the signal processing algorithms for Moving Target Indication (MTI) is provided. To verify the feasibility of the system implementation as well as test the developed signal processing algorithms, an experimental test bed was developed and the appropriate experimental campaign with the new Galileo satellites and a ferry as the target was carried out. The results confirm the system concept and its potential for multi-static operation, with the ferry being detected simultaneously by two satellites.**

***Index Terms*—Range Doppler processing, Maritime Moving Target Indication (M-MTI), passive radar, GNSS-based radar, Galileo.**

I. Introduction

THEutilisation of Global Navigation Satellite Systems (GNSS) as illuminators of opportunity for remote sensing is now well-established. Perhaps the most well-known technology in this area is GNSS-reflectometry (GNSS-R), with potential for Earth remote sensing applications. M. Martin-Neira et al. used the interferometric reception system to acquire the GNSS reflections and estimated the sea surface altimetry [1]. S. Vey et al. presented the GNSS signal-to-noise ratio (SNR) data to be used to estimate soil moisture at an intermediate scale of about 1000 m^2 as a long-term application, which has been achieved at the station Sutherland, South Africa, since 2008 [2]. J. F. Marchan-Hernandez et al. studied the relationship of the GNSS-R delay-Doppler maps (DDMs) and the sea state. They conducted field experiments and found that the DDM descriptor weakly affected by the GPS satellite geometry [3]. E. Valencia et al. proposed to use the DDM to retrieve the scattering coefficient of the sea surface, and this concept has been further applied for oil slick detection on the sea [4]-[5].

In the recent review papers [6] and [7], the GNSS-based system characteristics has been analyzed at large from the point of view of remote sensing applications. Suitable GNSS candidates for this kind of systems can be the Global Positioning System (GPS) [8], the GLObal NAvigation Satellite System (GLONASS) [9], Beidou [10], or the new European Galileo constellation [9], [11]. From a radar perspective, GNSS have been shown suitable for passive Synthetic Aperture Radar (SAR) systems on the theoretical and experimental level [9], [12], [13], with the ultimate goal of achieving persistent Earth observation and monitoring.

However, apart from the remote sensing and SAR applications, one of the areas now being investigated is the use of GNSS as transmitters of opportunity for a passive bistatic radar aimed at the detection of moving targets. This has already been considered and experimentally demonstrated for air targets such as airplanes, helicopters, etc. in forward-scattering in [14]. Moving to maritime targets the feasibility to use GNSS signals has been investigated in [15] considering GNSS-R technology. Concerning radar technologies, in [16] the use of GPS signals has been analyzed with specific reference to a configuration comprising transmitter, airborne receiver and target aligned on the same direction, so that a monostatic behavior of the target can be assumed; the reported results provide a theoretical confirmation of results in [17] where some experimental evidence of the detectability of a stationary target by means of GPS signals was given. This paper introduces the concept of maritime surveillance by means of GNSS-based passive radar systems in general bistatic acquisition geometries.

Traditionally, passive coherent location (PCL) radars for airborne or maritime target detection have relied predominantly on terrestrial signal sources, such as DAB/DVB-T [18]-[19], FM [20] and GSM [21]. These sources are attractive for a number of reasons. First of all, terrestrial base stations can guarantee a persistent monitoring of their surrounding areas, provided that a receiver is in the vicinity. In addition, their transmit powers are sufficiently high to achieve very long detection ranges. Moreover, their operating frequencies and, in some cases, their signal bandwidths (e.g. DVB-T [18]), allow the development of relatively straightforward receivers, as well as a sufficiently high resolution in Doppler and/or range for

radar purposes.

Nevertheless, all these transmitters of opportunity have a common drawback, which is that they are based on land. Because of this, and despite their long detection ranges, they still cannot provide coverage in areas such as the open sea. In such an environment, it is satellite emissions with a global or continental coverage which are sought after, with GNSS being one of very few signal sources available, while its maximum range resolution of 15m (using the Galileo E5a/b signals or the GPS L5) is comparable or even smaller than the dimensions of typical maritime targets.

Similar research for such applications has already been conducted for other satellites of opportunity, such as DVB-S [22]-[23] and Inmarsat [24]. However, the relative merit in using GNSS lies in their combination of global coverage, spatial diversity and waveform diversity. Every GNSS constellation provides the potential for persistent monitoring anywhere in the world, including the poles. Any point on Earth is illuminated typically by 6-8 satellites simultaneously from different angles if a single GNSS constellation is considered, so such point could be illuminated by 32 satellites when all 4 GNSS systems are in full capacity. Each satellite then transmits a number of signals, some of which are in different frequency bands, but all of which can be recorded by a single receiver as is the case for navigation receivers. Therefore, this is inherently a multi-static radar system where multiple signals could be combined to increase radar performance [25] or extend target information space [26].

The fundamental limitation in GNSS-based radar is its very restricted power budget. A single GNSS satellite has a low Effective Isotropic Radiated Power (EIRP), which substantially limits target detection range [14], [27]. This means that the power budget for a single signal of a single satellite is relatively poor. There is potential to combine multiple signals from multiple satellites to reinforce the total target power, while at the same time the clutter power can be suppressed due to both spatial and frequency diversity. In addition, placing receivers in the open sea, well beyond land and the coverage of shore-based maritime surveillance radars, substantially relaxes requirements on maximum detection range. However, the system optimization for coverage (may necessitate the use of a network of receivers) needs to be further considered. The system power budget study on the theoretical and experimental level, which includes Signal-to-Noise Ratio (SNR) improvement, limits on Coherent Processing Intervals (CPIs) for Moving Target Indication (MTI) [28]-[29] and clutter analysis [30]-[32] in this complex multi-static system is a subject for a dedicated research with long-term experimental campaigns and is hence beyond the scope of this paper.

The main objective of this paper is to investigate whether maritime MTI with bistatic GNSS-based radar is fundamentally possible, by assessing how GNSS signal reflections can be used for this purpose, developing the appropriate signal processing algorithms, and testing them with real data. In this experimental environment, the possibility of multi-static operation is also assessed. As a proof-of-concept study, the analysis presented here assumes a single signal from a single satellite, and for the experimental purposes, we have deliberately used targets with large Radar Cross Sections (RCS) at relatively short receiver stand-offs. In addition, in terms of signal processing, the analysis concentrates on the mechanics of identifying moving targets from GNSS signals as a first step in identifying the overall system feasibility, rather than the development of optimal signal processing algorithms for clutter/stationary target suppression, which are a subject for a dedicated study once the overall feasibility is confirmed.

The remaining content of the paper is organized as follows: Section II describes the GNSS-based radar acquisition geometry and signal model. On this basis, Section III and IV present the signal processing algorithms of the system, which are respectively the synchronization with regard to the Galileo E5a-Q signal and MTI processing algorithms. Next in Section V, experimental results are provided as the verification of the system feasibility and algorithm effectiveness.

II. GNSS-based Radar Geometry and Signal Model

The concept of the GNSS-based radar for maritime targets detection is shown in Fig.1. The transmitter is a GNSS satellite, while the receiver is above the sea. The receiver could be mounted on a buoy or on a balloon. The receiver itself is equipped with two channels. The Heterodyne Channel (HC) records the direct signal from all satellites in its field of view, used for signal synchronization between the receiver and the transmitters. The Radar Channel (RC) records the satellite echoes from the area of interest, which is used for MTI.

Comparing all the current available GNSS signal candidates, the Galileo E5 signal [11] is chosen as its bandwidth (10.23MHz) can provide one of the highest range resolutions possible (15m) with such a system. In this paper, we focus on the E5a-Q signal, however all analysis based on this is applicable for other GNSS signals too. The E5a-Q signal generation follows a tiered code construction, where a secondary code sequence is used to modify successive repetitions of the primary code. The simplified transmitted signal can be written as:

$$\boldsymbol{Y(t) = C_P(t)C_S(t)\cos(\omega_c t)}, \quad (1)$$

where $C_P(t)$ is the primary code of the E5a-Q channel and is a pseudorandom, orthogonal code. Its duration is 1 ms with chip rate (i.e., signal bandwidth) $f_{cr} = 10.23$ MHz. $C_S(t)$ is the E5a-Q secondary code, with a chip rate of 1KHz and a repetition period of 100 ms. The parameter $\omega_c = 2\pi \times 1176.45$ MHz is the carrier frequency of E5a-Q signal. Galileo operates on a Code Division Multiple Access (CDMA) protocol, which means that each satellite transmits its own primary and secondary codes, both of which are modulated using Bipolar Phase Shift Keying (BPSK). Between the two codes, the primary code is taken as the transmitted signal for GNSS-based radar because of its wider signal bandwidth, while the secondary code can be regarded as interfering with the primary code by shifting its phase by $\pm\pi$. It is also noted that despite the primary code is transmitted continuously, it does have a period of 1ms, which is referred to as the Pulse Repetition Interval (PRI) of the radar system hereafter.

After quadrature demodulation and radar data formatting, and ignoring constant phase and amplitude terms, the received signal at the HC can be written as:

$$s_0(t,u) = C_P[t-\tau_0(u)-\tau_e(u)]C_S[t-\tau_0(u)-\tau_e(u)] \times \exp\{j[2\pi f_{d0}(u)t+\varphi_0(u)+\varphi_e(u)]\}, \quad (2)$$

where $t \in [0, T_s]$ denotes fast-time, T_s is the PRI, $u \in [-T/2, T/2]$ is slow-time, and T is the dwell time on target. The parameters $\tau_0(u), \varphi_0(u)$ and $f_{d0}(u)$ are the instantaneous time delay, phase, and Doppler of the direct signal as functions of u, respectively. Their values depend on the relative position and movement between the satellite and the receiver. $\tau_e(u)$ and $\varphi_e(u)$ are the total delay and phase errors, respectively, induced by atmospheric factors as well as receiver artefacts such as clock cycle slips and local oscillator drift.

Since the receiver-target distance (a few km) is incomparably less than the transmitter-target distance (>20,000km), atmospheric errors between the direct and reflected signals are similar and can therefore be compensated to an adequate level. At the same time, within the receiving system, the HC and RC use the same clocks and local oscillators, and therefore the same clock cycle slips and local oscillator drift can be expected for the two channels.

Likewise, assuming one single target, the RC signal can be written as:

$$s(t,u) = C_P[t-\tau(u)-\tau_e(u)]C_S[t-\tau(u)-\tau_e(u)] \times \exp\{j[2\pi f_d(u)t+\varphi(u)+\varphi_e(u)]\}, \quad (3)$$

where $\tau(u), \varphi(u)$ and $f_d(u)$ are the instantaneous time delay, phase, and Doppler of the target reflected signal. Their values are related to the bistatic range, which is the instantaneous range from the satellite to the target and the target to the receiver.

III. Overview of Signal Synchronisation

The initial phase of the satellite transmitted signal and the start of the E5a-Q code (3) is the fundamental information required for extracting target information in range and Doppler. As mentioned in Section II, both parameters above are affected by atmospheric and receiver errors, however these errors are common to the HC and the RC. Therefore, they can be extracted from the HC and compensated in the RC to enable coherent processing. On the other hand, at the output of the HC antenna the SNR can be as low as -30 dB [9], considering a low-gain (~6dB) antenna and signal filtering. For this reason a signal synchronization algorithm is needed, which tracks the direct signal in delay, Doppler and phase, and uses these parameters as a reference for the reflected signal in the RC.As the reference signal, the direct signal parameters (delay, Doppler due to relative motion between the transmitter and the receiver, and phase) from the satellite, recorded at the HC, can be used.

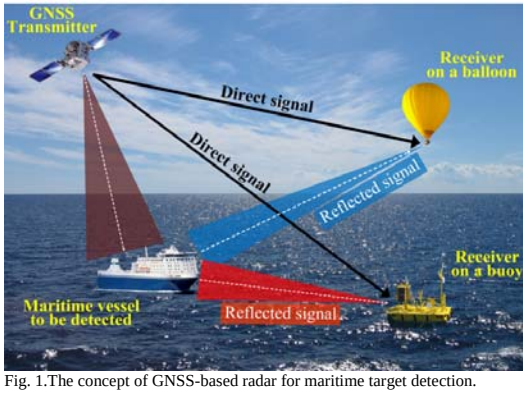

Fig. 1.The concept of GNSS-based radar for maritime target detection.

Fig.2 presents a block diagram of the synchronization algorithm used for the purpose above. It is based on a popular GNSS tracking algorithm – the Block Adjustment of Synchronizing Signal (BASS). The algorithm operates with

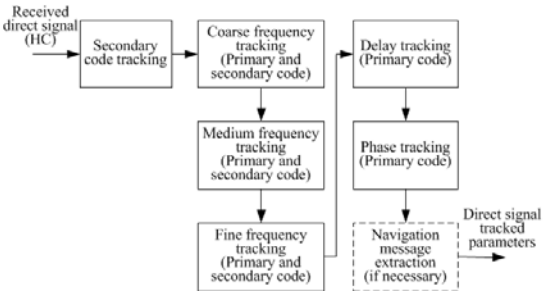

Fig. 2.Synchronisation algorithm for GNSS-based radar.

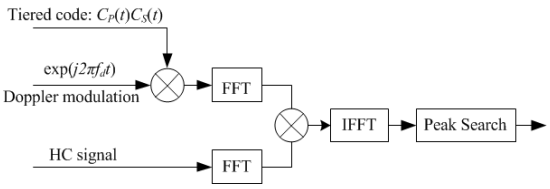

Fig. 3. Secondary code tracking block diagram for one single Doppler frequency.

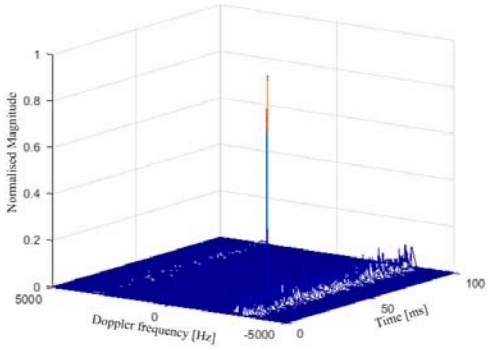

Fig. 4. Secondary code tracking output for 100 ms data. The location of the peak indicates the start number of the secondary code and the corresponding Doppler frequency.

data recorded on the HC to track the direct signal delay, Doppler, and phase in every PRI. To reduce computational load, Doppler is tracked in three stages, termed as coarse, medium and fine. The general application of this algorithm for GNSS-based radar has been described extensively in [9], so only a brief overview is provided here. The key difference here is that for the Galileo E5 signals, both the secondary and the primary code should be tracked from the HC before the secondary code is removed from the RC. The synchronization process is briefly described in the next paragraphs.

Since the secondary code is a known pseudo-random sequence, its start can be found with a matched filtering method. The reference signal is the 100ms tiered code consisting of both the primary and secondary codes, $C_P(t)C_S(t)$, with variable Doppler modulation components $\exp(j2\pi f_{d0}t)$, where $f_{dk} = -5000 + k \times 1000$ Hz, with $k = 0,1,2,..10$ to provide a coarse estimate of the Doppler frequency of the direct signal as well as the time delay associated with the start of the secondary code. Fig.3 shows the matched filtering block diagram for one single Doppler frequency.

Fig.4 gives an example output of the above process. Matched filtering was applied to the first 100 ms experimental data for all Doppler frequencies f_{dk}. The location of the peak indicates that the first PRI of the experimental data corresponds to the n-th code chip in a secondary code period, as well as the direct signal Doppler. The presence of smaller peaks along the range bin corresponding to the estimated Doppler, which are the side-lobes in the correlation function of the secondary code, are also noted.

Having recovered the start of the secondary code, $C_S(t)$ can be removed from (3). Based on the tracked start epoch of the tiered code, we can apply the typical 3-step Doppler frequency tracking, from coarse to medium then to fine frequency tracking as in [5].

With the tracked Doppler, the accurate matched filtering can be applied to track delay and phase of the primary code in direct signal.

Fig.5 shows the tracked Doppler, delay and phase of a 2 mins long direct signal at the output of the synchronization algorithm discussed above.

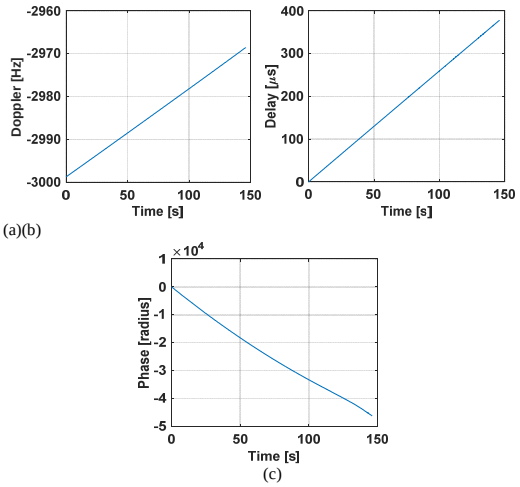

Fig. 5. Tracking output of direct signal synchronization: (a) the direct signal Doppler, (b) the direct signal delay and (c) the unwrapped direct signal phase.

With the tracked parameters, the phase error terms $\varphi_e(u)$ in (2) can be extracted. Hence, we can generate the local reference signal for the following range compression for RC signal, as well as the corresponding phase error compensation signal:

$$s_{\text{ref}}(t,u) = C_P[t - \tau_0(u) - \tau_e(u)]C_S[t - \tau_0(u) - \tau_e(u)] \times \exp\{j[2\pi f_{d0}(u)t + \varphi_0(u)]\}. \quad (4)$$

$$s_{\text{pe}}(t,u) = \exp\{j[-\varphi_e(u)]\}. \quad (5)$$

The proposed process therefore tracks the secondary code, Doppler frequency, time delay and phase of the direct signal as the synchronization output, for the E5a-Q signal. The same applies to E5b-Q, while for the non-pilot channels, E5a-I and E5b-I, an extra step needs to be involved for navigation message extraction, achieved by detecting the phase transition due to the navigation code bit inversion [9].

Comment [F1]: I think it should be f_dk. Please check.

IV. MTI Processing Technique

The goal of MTI is to identify moving objects in the field of view of the RC antenna. The received signal contains reflections from the observed area, including fixed and moving targets as well as sea clutter, however those can be distinguished in terms of their range and Doppler frequency.

Therefore, the objective is to identify the presence of a target and localise it in range and Doppler. For this purpose, a MTI technique is proposed to properly integrate target returns, thus

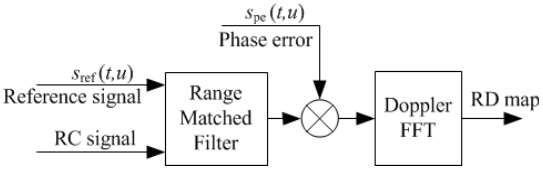

Fig. 6.Basic moving target indicator (MTI) algorithm.

compressing target echoes in the bistatic range and bistatic Doppler plane. Considering the low EIRP of the exploited transmitter of opportunity very long integration time intervals can be needed to detect low/medium RCS targets. In contrast, relatively short integration times suffice for high RCS target detection. On this basis, the proposed MTI processing comprises two stages: 1) basic MTI for short time integration allowing for high RCS target detection; 2) advanced MTI for long time intergation potentially enabling low/medium RCS target detection.

A. Basic MTI processing

The signal processing procedure to identify the presence of a high-RCS target in range and Doppler is based on matched filtering and is shown in Fig.6. Based on the signal synchronization outputs described in Section III, a reference signal that is a noise-free replica of the direct signal is constructed for matched filtering in the range direction with the collected radar data. After this operation, data are re-arranged into the equivalent of a fast-time (range), slow-time (Doppler) matrix, followed by a Fast Fourier Transform (FFT) in the slow-time direction. The FFT can separate targets and clutters with different Doppler characteristics with the appropriate signal processing gain, for which a suitable Coherent Processing Interval (CPI) should be identified. At the output of the algorithm, a range-Doppler (RD) map is produced. Despite the fact that this system is considered from a bistatic radar point of view, there are synergies with work on GNSS-R, where DDM's instead of RD maps are traditionally used. The two types of outputs are essentially equivalent by the appropriate transformation from delay to range.

The range compressed data are given by the correlation function between the reflected signal $s(t,u)$ in (3) and the local reference signals$s_{\mathrm{ref}}(t,u)$ in (4) thus obtaining:

$$rc(t,u) = R_{cf}[t-\Delta\tau(u)] \times \exp\{j[2\pi\Delta f_d(u)t + \Delta\varphi(u)]\}, \quad (6)$$

with$R_{cf}(\cdot)$being the amplitude of the cross-correlation function of $s_{\mathrm{ref}}(t,u)$ and $s_{RC}(t,u)$. The quantities $\Delta\tau(u), \Delta\varphi(u)$ and $\Delta f_d(u)$are the instantaneous difference between the direct and reflected signal in terms of time delay, phase, and Doppler respectively, and therefore can be calculated by:

$$\Delta\tau(u) = \tau(u) - \tau_0(u). \quad (7)$$

$$\Delta f_d(u) = f_d(u) - f_{d0}(u). \quad (8)$$

$$\Delta\varphi(u) = \varphi(u) - \varphi_0(u). \quad (9)$$

Then, through the FFT in the slow-time dimension and converting the fast-time dimension into bistatic range as $\Delta\tau = \Delta r/c$, we can get the target reflected signal in the RD domain (r, f_u) as:

$$RD(r,f_u) = R_{cf}\{t - [\Delta r(\Delta f_{dc})/c]\} \times W_a(f_u - \Delta f_{dc}) \times \exp\{j\theta_a(r,f_u)\}, \quad (10)$$

whereΔf_{dc} is the Doppler centre of $\Delta f_d(u)$ during the FFT processing interval. $\Delta r(\Delta f_{dc})$ is the relative bistatic range of the target with the subtraction of the baseline. $W_a(f_u - \Delta f_{dc})$ is the spectral envelope centred at Δf_{dc}. $\theta_a(r,f_u)$ is the phase angle after FT.

The coherent integration accomplished by the FFT should be sufficient to detect high-RCS targets, whereas low-RCS targets cannot be extracted from the background by the basic MTI. To face this problem the second stage performs a proper integration of multiple RD maps obtained by the first stage over multiple consecutive time interval, as explained below.

B. Long integration time MTI processing

While range and Doppler migration can be considered negligible at the single RD map level due to the coarse range resolution and the short integration time, the same does not apply when a long integration time is involved: indeed the moving target will migrate, changing its position in the RD maps relative to successive time intervals. Obviously, such migration has to be compensated to align target contributions in order to perform a proper integration: in this way, the target energy is correctly concentrated and a proper signal to disturbance power ratio level is recovered enabling target detection. To this aim, the second stage comprises two steps:

1) target motion compensation (TMC): this step receives in input a sequence of N RD maps, obtained by the basic MTI over N consecutive time batches of duration T_B, and provides in output a sequence of compensated RD maps where range and Doppler migration correction has been applied according to a specific Doppler rate value;

2) compensated RD maps integration: the second step receives in input the sequence provided by the first one and performs a non-coherent integration of the corrected RD maps.

The range and Doppler migration compensation step basically aligns the n-th RD map, $RD_n(r,f_u)$ with $n = -N/2 \ldots N/2-1$, to the reference map assumed as the $n=0$ map (namely the central map in the sequence to be integrated).The migration correction is based on the assumption that a moving target located in $(\Delta r^0, \Delta f_{dc}^0)$ in the reference map when observed in the n-th map experiences a range migration given by:

$$\Delta r^{n-0}(\Delta f_{dc}^n, \dot{f}_{dc}^*) = \Delta r^n - \Delta r^0 = -\lambda\left[(\Delta f_{dc}^n - \dot{f}_{dc}^* nT_B)nT_B + \frac{\dot{f}_{dc}^*(nT_B)^2}{2}\right], \quad (11)$$

and a Doppler migration given by:

$$\Delta f_{dc}^{n-0}(\dot{f}_{dc}^*) = \Delta f_{dc}^n - \Delta f_{dc}^0 = \dot{f}_{dc}^* nT_B, \quad (12)$$

being $(\Delta r^n, \Delta f_{dc}^n)$the target position in the n-th map and $\dot{f}_{dc}^*$the Doppler rate value under test. Range migration can be therefore compensated by multiplying the n-th map in the (range frequency, Doppler frequency) domain by the phase term corresponding to (11), thus obtaining:

$$RD_n^{RC}(r,f_u,\dot{f}_{dc}^*) = RD_n[r - \Delta r^{n-0}(f_u,\dot{f}_{dc}^*), f_u], \quad (13)$$

while Doppler migration can be compensated by multiplying the n-th range corrected map in the (range, slow-time) domain by the phase term corresponding to (12), thus obtaining:

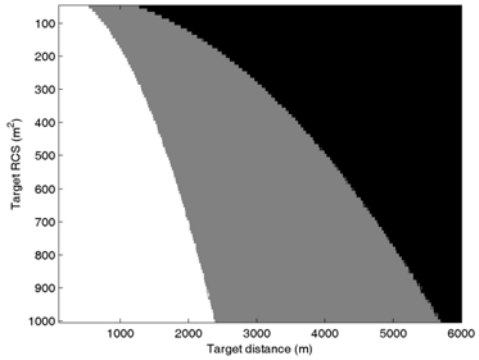

Fig. 7.Detection performance as a function of the target RCS and distance from the receiver for $P_{fa}=10^{-3}$.

$$RD_n^{RCDC}(r, f_u) = RD_n^{RC}\left[r, f_u - \Delta f_{dc}^{n-0}\left(\dot{f}_{dc}^*\right), \dot{f}_{dc}^*\right]. \quad (14)$$

Once the migration correction has been performed, the target is located in the same position in the maps so that its returns can be properly integrated. Taking into account the very long integration time involved (up to several tens of seconds), a non-coherently integration strategy is performed to cope with possible fluctuations of the target complex reflectivity. Therefore, integration is obtained by means of:

$$RD_{int}\left(r, f_u, \dot{f}_{dc}^*\right) = \frac{1}{N}\sum_n \left\| RD_n^{RCDC}\left(r, f_u, \dot{f}_{dc}^*\right)\right\|. \quad (15)$$

A completely adaptive technique can be obtained by considering a bank structure with different branches in the bank performing steps 1-2 according to different values of the Doppler rate chosen by fixing a reasonable range of target velocities (including the "zero velocity") and by knowing the overall integration time [33]. The presence of possible movers can be sought in the integrated map thanks to the recovery of suitable signal to background power ratio values.

Indeed, the integration process brings the energy of the target echoes at the top of its concentration and gain. At the same time, it reduces the fluctuations of the extended disturbance background thanks to the averaging over long time intervals. Moreover, it should also lower the level of possible point-like disturbance by spreading it thanks to the processing matched to the target motion. It is also worth mentioning that such point-like returns could be also easily filtered out when sufficiently close to the zero Doppler frequency or, as an alternative, they could be identified and removed by applying an ad-hoc strategy as for example in [33].

As it was mentioned in Section I, a complete characterization of system performance would require the optimisation of a number of system parameters, which is beyond the goal of this paper. However, as a first means of understanding performance enhancement due to the TMC, we propose here a simple analysis based on our experimental parameters and equipment.

In particular, for the analysis we refer to the E5a Galileo transmission[11], and assume the receiving system having a surveillance antenna with area 0.195 m^2 and efficiency 0.7, noise figure 1.5 dB and system losses 6 dB (values corresponding to the prototype used in the experimental campaign). In agreement with the experimental results presented in Section V, a coherent processing interval (single batch T_b) set to 2.5 s is used for the basic MTI while 50 s (namely 20 batches) are integrated by the advanced technique implying the use of a bank with M=132 branches. Fig.7 shows the values of target RCS (Swerling 0 target model, but similar results could be shown for Swerling I) and distance from the receiver assuring a detection probability equal to or higher than 0.75 keeping the final false alarm rate equal to 10^{-3} (about P_{fa}/M has to be guaranteed at the single branch of the bank when a 1-out-of-M logic is applied). In the figure, the white area represents the values satisfying the requirement when detection is performed at the single batch level, while the union of white and gray areas represent the values corresponding to detection performed by means of the advanced technique; the black area represents conditions where a detection probability lower than 0.75 is obtained. It can be observed that the identification of a composite integration strategy allows the recovery of signal to background power ratio values enabling target detection otherwise inhibited. For example, without TMC a target with RCS=300 m^2 cannot be detected at ranges higher than 1300 m, whereas the TMC allows increasing its maximum detection range up to 3200 m.

V. Experimental Confirmation

A. Experimental Setup and Parameters

Maritime experiments were planned and conducted using Galileo satellites as transmitters of opportunity and the passive receiver situated at the eastern coastal area of Plymouth harbour in UK. Target of opportunity was the commercial Brittany ferry running in schedule. Fig.8 (a) shows the data acquisition geometry during the measurement.

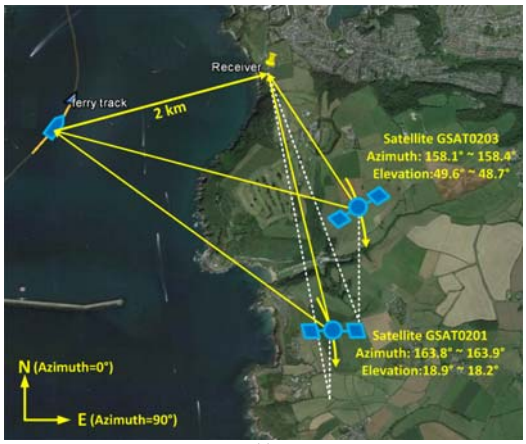

(a)

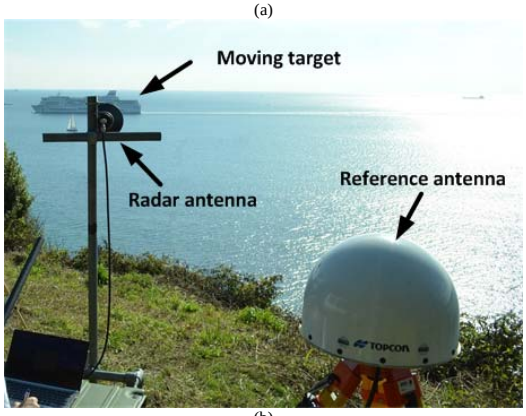

(b)

(c)

Fig. 8. (a) Schematic diagram of the experimental GNSS-based radar data acquisition geometry, (b) the experimental setup of the receiving system and (c) the optical photograph of the ferry.

The experimental receiver of GNSS-based radar [Fig.8 (b)] contains two RF channels for recording HC and RC signals, respectively. The HC uses a low-gain antenna to record the direct signal from all available satellites, while the RC uses a high-gain antenna to acquire the weak echoes from the area of interest.

TABLE I
EXPERIMENTAL AND SIGNAL PROCESSING PARAMETERS

Parameter		Value
Sat 1	Number	GSAT0201
	Ranging code	PRN18 (E5a-Q primary code)
	Bistatic angle	97° ~ 85°
	Azimuth(relevant to North)	163.8° ~ 163.9°
	Elevation(relevant to HC antenna)	18.9° ~ 18.2°
Sat 2	Number	GSAT0203
	Ranging code	PRN26 (E5a-Q primary code)
	Bistatic angle	91° ~ 83°
	Azimuth(relevant to North)	158.1° ~ 158.4°
	Elevation(relevant to HC antenna)	49.6° ~ 48.7°
Carrier frequency		1176.45MHz
Sampling frequency		50 MHz
Dwell time		145 second
Pulse repetition interval		1millisecond
Coherent processing interval		2.5 second
Non-coherent processing interval		10 second

Fig.8 (c) gives a photograph of the ferry taken during experiments. The length of the ferry is approximately 184 m, and its beam is 25 m. The real track of the ferry was found in the Automatic Identification System (AIS) and used as the ground truth for comparison with the experimentally tracked results. Two satellites in view of the receiver were successfully synchronized. Their azimuths and elevations were marked in Fig.8 (a). The experimental parameters are shown in Table I, as well as the specific parameters used for signal processing.

B. MTI Processing Results

Since the signal transmitted by different satellites can be extracted using the corresponding Pseudo Random Noise (PRN) codes, the signal processing discussed in Section III and IV can be separately applied to different satellites, and then the RD maps for certain integration period can be obtained. The appropriate CPI was found by progressively increasing coherent integration times, and taking the maximum time for which the signal processing gain due to matched filtering increased linearly. For our experimental parameters, the CPI found with this method was 2.5s. Fig.9 (a) gives the RD map for satellite 1 (GSAT0201), where the ferry can be seen clearly as a strong scattering point. The colour scale is in dB, where 0 dB is the highest echo intensity in the map. This point is located at zero bistatic range and zero bistatic Doppler, and is the compressed direct signal recorded in the RC. Along the zero-Doppler line the sidelobes of the compressed direct signal can be seen. Fig.9 (b) gives the result of a non-coherent summation of 4 sets of adjacent coherently processed RD maps. Hence, the occupied data interval of (b) is 10 s. It should be noted here that in our RD maps, the direct signal at zero Doppler has not been filtered out, as one would expect from a traditional MTI. This is because in this case it can be used as a reference for understanding the relative strengths of the target and the clutter. Fig.10 shows cross-sections of Fig.9 (b), with regard to the ferry and for range and Doppler directions respectively. The corresponding results for satellite 2 (GSAT0203) are given in Fig.11 and Fig.12.

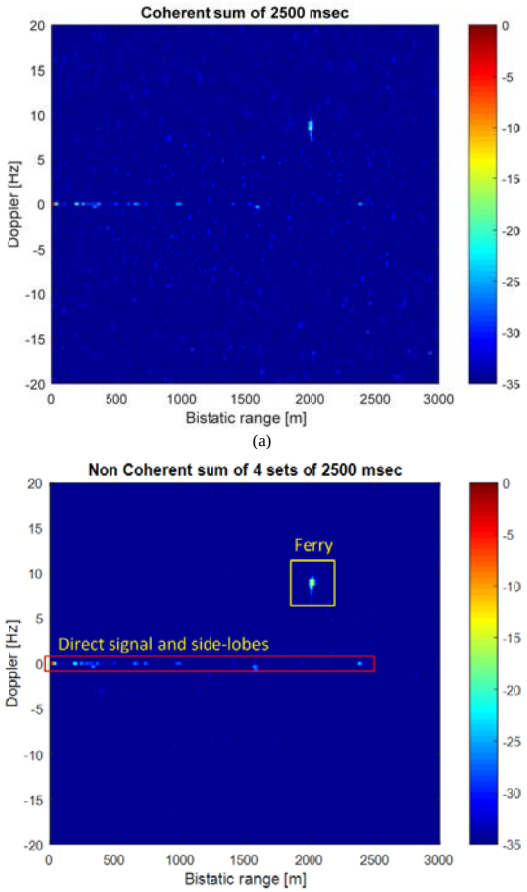

Fig. 9.Experimental results of satellite 1: (a) RD map of 2.5 s coherent integration time (b) non-coherent summation of 4 sets of adjacent RD maps, with a total data acquisition time of 10 s.

The results in Fig.9-Fig.12 have been obtained from a selected 10 s long interval providing good characteristics in terms of signal to background ratio. Moreover, within such interval, it could be shown that the target exhibits an almost constant Doppler frequency, i.e. a negligible Doppler rate. In accordance with (11)-(12), this entails only a linear range migration, whereas range curvature and Doppler migration are absent. In order to illustrate the capability of the advanced MTI technique to increase the detection performance of the passive radar system under consideration, a different and longer time interval is selected. A data stream of 50 s centered on 60 s from start acquisition time is selected from acquisition of satellite 2, because, as it will be discussed later, it provided the worst signal to background ratio. Within this interval, the target Doppler frequency is no more constant, resulting in a Doppler rate different from zero.

This interval is segmented in consecutive batches 2.5 s long, and the resulting 20 RD maps are then integrated. The obtained integrated maps are shown in Fig.13. Maps are expressed in dB and each map has been normalized to its maximum value. Fig.13 (a) shows the map obtained by directly integrating the set of RD maps, i.e. by skipping the TMC step. As it is apparent, the motion of the target entailed a range and Doppler migration over the long integration time, resulting in a spread of the target energy over different range-Doppler cells of the integrated map. The map obtained by considering also the TMC and provided by the branch of the bank providing best matching with the target kinematic is shown in Fig.13 (b). As evident, the advanced MTI technique has been able to properly integrate the target contributions in the individual maps repositioning them in the same location, thus providing a higher energy concentration. This can be well observed looking at the bottom boxes of Fig.13, highlighting the target position (it should be pointed out that, for sake of better visualization, the zooms have displayed with a color scale with 10 dB of dynamic normalized to the peak value of the ferry return in the TMC integrated map). Because of the enhanced energy concentration provided by the TMC, a gain in terms of signal to background ratio can be obtained, as evidenced by looking at the range and Doppler cuts around the target peak position of the compensated map in Fig.14.

A second important benefit arising from the TMC procedure concerns the clutter. Indeed, if on one hand the Doppler rate-based processing allows building up the useful signal energy, on the other hand it reduces the amount of clutter energy per cell by spreading it over multiple cells, as it is apparent looking at the sea clutter returns highlighted in Fig.13 and the corresponding Doppler cuts in Fig.15.

It should be pointed out that this specific acquisition does not strictly require a very long integration time to make the target detectable, because it concerns a target with high size and high RCS. Moreover, since it concerns a not particularly fast target, range and Doppler migrations are not relevant over few consecutive RD maps therefore allowing a proper integration of some RD maps also by skipping the TMC procedure. However, previous results show the general validity of the advanced MTI technique in this particular kind of a passive radar system. Indeed, if targets with low RCS were acquired by the system, integration over several tens of seconds accomplished with the TMC step would be mandatory to obtain an improvement of SNR able to make the detection possible.

C. MTI Results Analysis

From the results in Fig.9-Fig.11, the target reflected signal from satellite 1 shows high concentration on one scattering point, while with regard to the reflection from satellite 2, the target performs more like gathering of a series of scattering points, and in Fig.12 (a), the target's response in range has a high coincidence with the ferry dimension in length. This additional information is due to satellite spatial diversity and could be used in the future to estimate the physical dimensions of the target. The different target responses shown for two satellites (see Fig.9 and Fig.11) arise from the different bistatic angles and the different RCS of the target by looking from different directions. For the entire dwell time of 145 s of this dataset, by processing every 10 s data with an interval of 1 s, we have obtained 136 RD maps. The processing block diagram is shown in Fig.16. By this process, the RD histories for two satellites are obtained separately and shown in respectively Fig.17 and Fig.18.

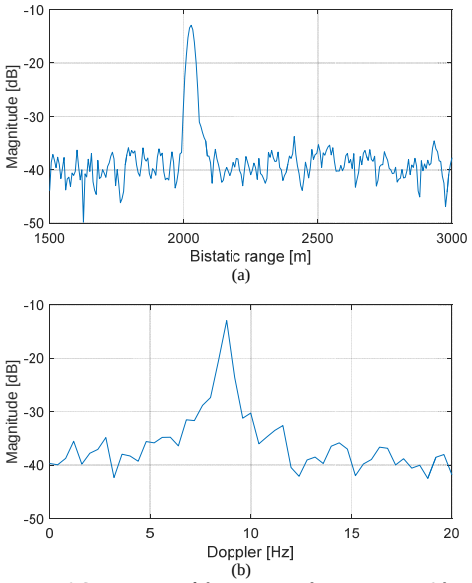

Fig. 10.Cross-sections of the experimental RD map in Fig.9-b: range (a) and Doppler (b) cross-sections of the target.

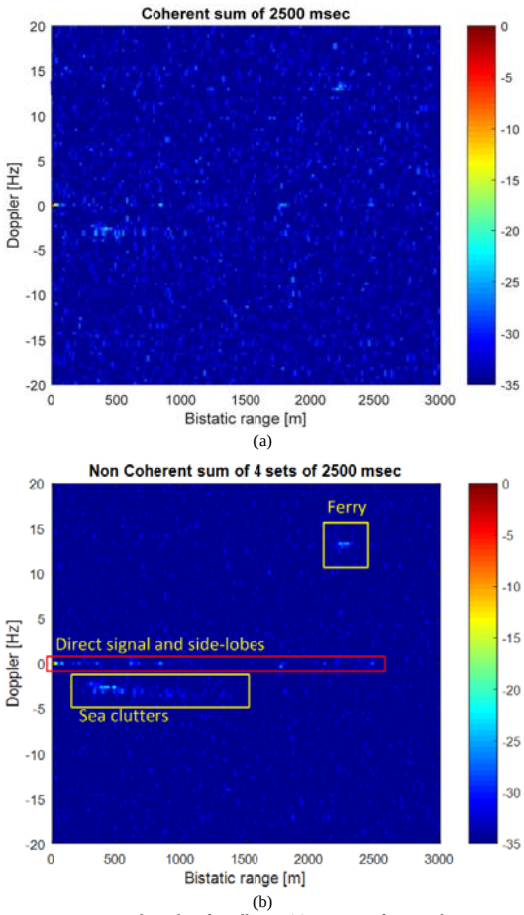

Fig. 11.Experimental results of satellite 2: (a) RD map of 2.5 s coherent integration time (b) non-coherent summation of 4 sets of adjacent RD maps, with a total data acquisition time of 10 s.

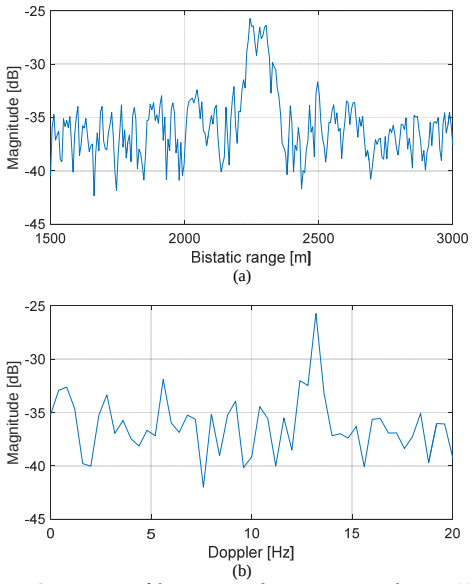

Fig. 12.Cross-sections of the experimental RD map in Fig.11-b: range (a) and Doppler (b) cross-sections of the target.

With the obtained RD history, for every point of slow-time, corresponding RD map can be obtained, from which we can determine the simultaneous bistatic range and bistatic Doppler by the peak value of the target echoes in both directions. Since those are different for each satellite, it stands to reason that the system provides information that could be used for multi-static operation.

Fig.19 (red curve) gives the variation of the bistatic range versus time for satellite 1. In our case, interval of adjacent samples in range dimension means 6 m in distance, so the detected bistatic range (red curve) is in multiples of 6 m. The AIS data obtained for the target can be used as the ground truth, hence in Fig.19 the calculated bistatic range (blue curve) using AIS data is given for comparison. Likewise, Fig.20 gives the Doppler variation with changing of time for satellite 1.

From Fig.19, the changing trend of the detected bistatic range agrees very well with the expected values by AIS data, whose positional accuracy is similar to that of satellite navigation receivers. According to the parameters in Table I, we can calculate the bistatic range resolution is around 30 m. It can be seen that the absolute value of this difference is always smaller than one range resolution cell. It should be noted that the detected track records the location of the strongest scattering point on the target, while the ground truth gives records of the location of AIS data logger. Considering that our target is a ~200m ferry, these two tracks can be essentially different. For the same reason, differences between measured and predicted values cannot take into account maneuvers of the ferry as it was entering port at the time of measurement.

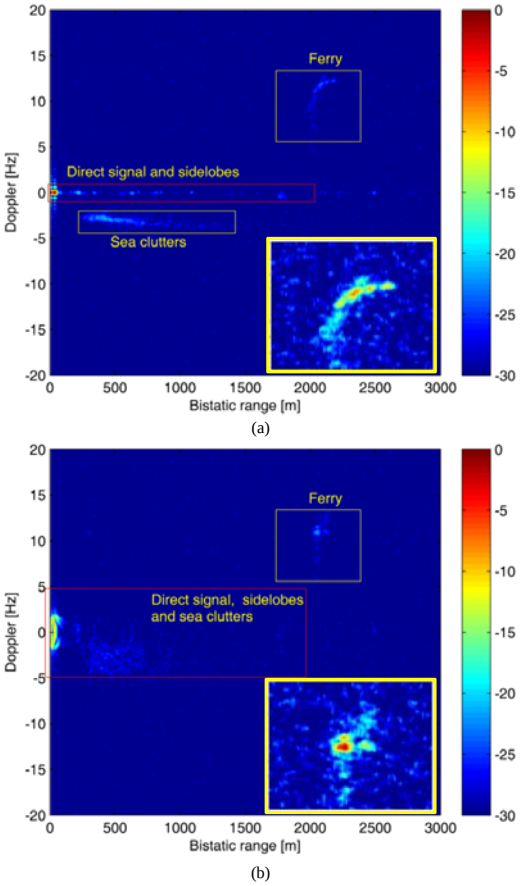

Fig. 13.Experimental results of satellite 2 -integration of 20consecutive RD maps with (a) and without (b) target motion compensation, with a total data acquisition time of 50 s.

Apart from the instantaneous range and Doppler parameters, differences in echo intensity can be observed between the two acquisitions relative to the direct signal in Fig.17 and Fig.18. A comparison between the two figures shows that for satellite 1, the target signal strength is higher compared to the direct signal than for satellite 2, while clutter strength in the case of satellite 1 is lower than that of satellite 2. This indicates that there exist optimal satellite positions that maximize signal strength while minimizing clutter strength, and this is a direct result of spatial diversity, to be explored more in the future.

Correspondingly, Fig.21 and Fig.22 present the detected bistatic range and bistatic Doppler for satellite 2, also with values calculated from AIS data as comparison. The absolute value of the difference of curves in Fig.21 is always smaller than one and a half range resolution cell.

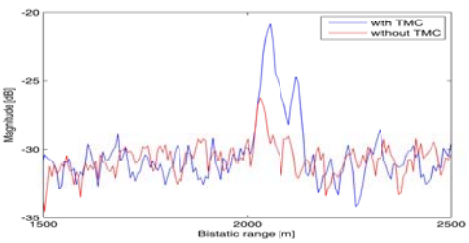

(a)

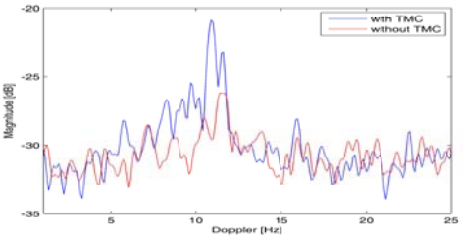

(b)

Fig. 14.Experimental ferry range (a) and Doppler (b) cross-sections for the advanced MTI technique.

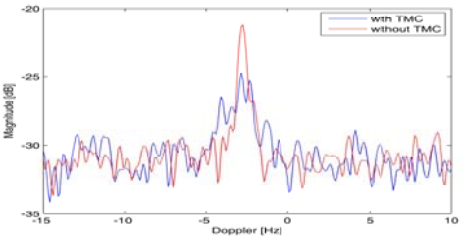

Fig. 15.Doppler cross-sections of the sea clutter background.

Because of its high RCS, the considered target becomes visible above clutter level for both satellites integrating over limited observation times where, depending also on the particular target kinematic parameters, the TMC is not essential. However, when targets with lower RCS are considered, the increasing of the observation time is needed to assure super-clutter visibility conditions, and in such a case the TMC step is mandatory, as discussed in previous section. In Fig.19-Fig.21, a second set of RD histories is shown (black curves) by considering the following processing. Referring to the block diagram in Fig.16, by setting CPI = 2.5 s and NCPI = 20 × 2.5 s = 50 s, a total of N = 96 integrated maps are obtained by considering the integration of the compensated RD maps accounting for the nominal value of the Doppler rate. As it is apparent, the scatterer plots obtained from the advanced MTI technique show a lower dispersion of the target tracks than the

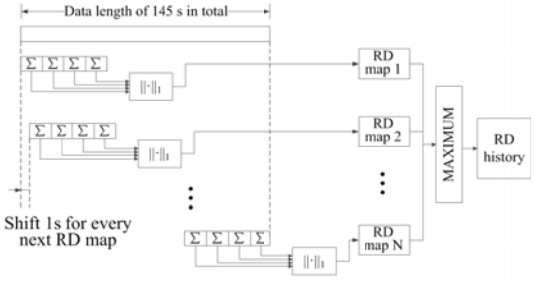

Σ: represent a coherent integration of 2.5 s

$\|\cdot\|_1$: is the 1-norm, here it is used to denote non-coherent summation of 4 sets of 2.5 s

MAXIMUM: means applying a max(·) operator for each RD pixel among all the values at the same pixel from N RD maps

Fig.16.Processing of RD history.

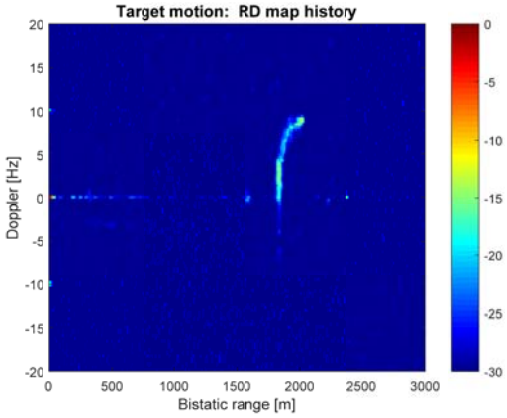

Fig.17.Range-Doppler history over 145 s dwell time of satellite 1.

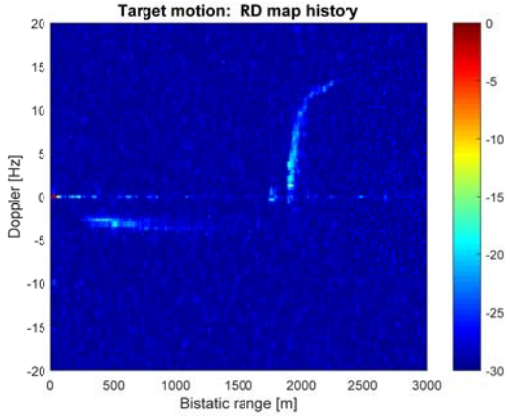

Fig.18.Range-Doppler history over 145 s dwell time of satellite 2.

corresponding plots resulting from the basic MTI, because of the enhanced concentration of the target energy provided by the TMC step. Table II compares the Root Mean Square (RMS) of the range and Doppler difference from the calculated and AIS tracks obtained in the previous case (integration of 4×2.5 s RD map without TMC) and with this advanced processing. The RMS values have been evaluated over the same time interval for the basic and the advanced processing case and we can observe that, for both the satellites, the advanced processing provided smaller differences among the calculated tracks and the AIS ground truth. This analysis further demonstrates the effectiveness of the advanced MTI technique to collect the signal energy over long integration times, being a mandatory condition to counteract the restricted power budget provided by GNSS. It is worth to point out that, despite the high target energy concentration enabled by the advanced MTI processing, a visible fluctuation of the detected tracks can be observed around specific time intervals (e.g., bistatic Doppler in Fig.20 in the interval [100-120] s). It could be shown that such behaviour is related to the large size of the considered target. In fact, depending on the particular target orientation, position and acquisition geometry, multiple scattering points could be observed [as shown in Fig.12 (a)] and this can cause a dispersion of the tracks. In those situations where the target does not behave like a single scattering point, the combined use of the advanced MTI algorithm and the spatial diversity arising from the exploitation of multiple satellites may provide the additional capability for the system to extract features of the detected ship, which will be the focus of future steps of our research.

TABLE II. RMS DIFFERENCES FROM THE CALCULATED AND AIS RANGE AND DOPPLER TRACKS

satellite	processing	range RMS	Doppler RMS
1	basic	18.4 m	1.9 Hz
	advanced	13.2 m	1.5 Hz
2	basic	23.5 m	2.0 Hz
	advanced	10.6 m	1.5 Hz

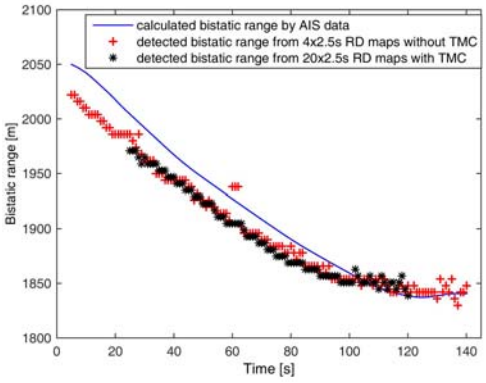

Fig.19.Comparison of bistatic ranges for satellite 1.

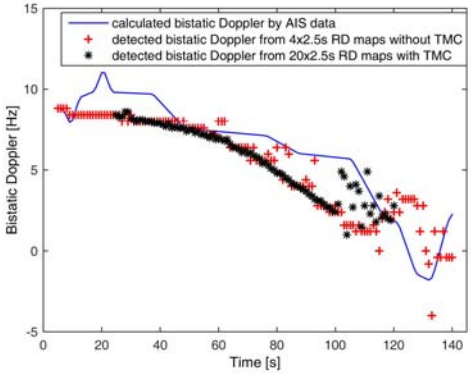

Fig.20.Comparison of bistatic Doppler frequencies for satellite 1.

VI. CONCLUSION

In this paper, we have exploited the potential of using GNSS as transmitters of opportunity for maritime moving target indication. Due to the global coverage of GNSS constellations, the proposed concept can be effective to potentially fill gaps of signal sources in areas such as the open sea.

Our proof-of-concept study was based on the maritime GNSS-based radar system implementation followed by experimental trials. Within this remit, signal processing algorithms were derived, including synchronisation processing and MTI processing.

One set of data acquisition was successfully recorded with Galileo E5a-Q signal under a maritime environment and with one commercial ferry passing through. By applying the proposed algorithms, we have obtained MTI results throughout the 2-min data records. The ferry has been successfully detected by two Galileo satellites simultaneously. Both experimental results of two different satellites have accurately indicated the motion of the ferry, which coincide with the ground truth in a high degree, confirming the feasibility of the system under ideal but real conditions as well as the functionality of the signal processing algorithms used.

In addition, the feasibility of a long time integration MTI processing has been preliminary demonstrated, thus indicating the potential of this approach to increase the detection performance of the proposed passive radar system, likely allowing the detection of low observable targets. Furthermore, the results show the system provides sufficient information to consider and test multi-static passive radar techniques based on GNSS.

Having shown that GNSS-based radar signals can be used to identify the presence of moving maritime targets, the next steps in the system feasibility study are the comprehensive system power budget evaluation, the upgrade of RD algorithms to MTI schemes, and the investigation of the system's potential for multi-static operation.

Acknowledgment

This project has received funding from the European GNSS Agency under the European Union's Horizon 2020 research and innovation programme under grant agreement No 641486, "GALILEO-BASED PASSIVE RADAR SYSTEM FORMARITIME SURVEILLANCE — spyGLASS". The first spyGLASS prototype is an experimental van-mounted system designed and developed by Aster S.p.A. and ElettronicaGmbh.

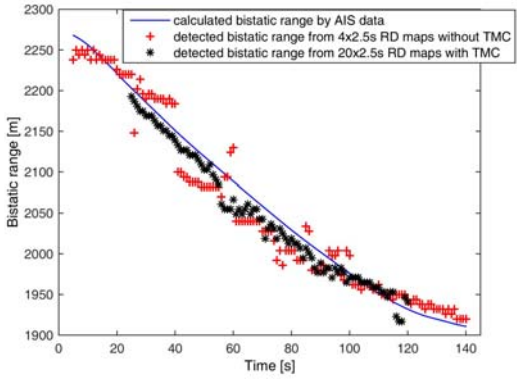

Fig.21.Comparison of bistatic ranges for satellite 2.

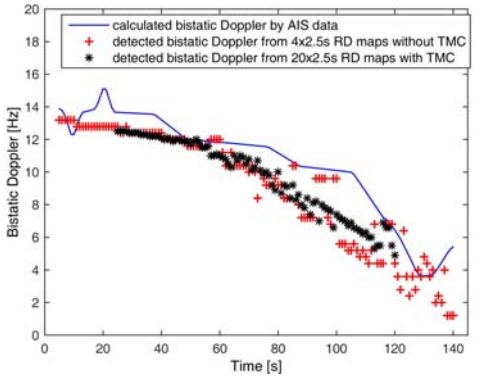

Fig.22.Comparison of bistatic Doppler frequencies for satellite 2.

REFERENCES

[1] M. Martin-Neira, M. Caparrini, J. Font-Rossello, S. Lannelongue, C. S. Vallmitjana, "The PARIS concept: An experimental demonstration of sea surface altimetry using GPS reflected signals," in *IEEE Trans. Geosci. Remote Sens*., vol. 39, no. 1, pp. 142-150, Jan. 2001.

[2] S. Vey, A. Güntner, J. Wickert, T. Blume, M. Ramatschi, "Long-term soil moisture dynamics derived from GNSS interferometric reflectometry: A case study for Sutherland, South Africa," in *GPS Solutions*, pp. 1-14, Jul. 2015.

[3] J. F. Marchan-Hernandez, E. Valencia, N. Rodriguez-Alvarez, I. Ramos-Perez, X. Bosch-Lluis, A. Camps, F. Eugenio, J. Marcello, "Sea-state determination using GNSS-R data," in *IEEE Geosci. Remote Sens. Lett.*,vol. 7, no. 4, pp. 621-625, Apr. 2010.

[4] E. Valencia, A. Camps, J. F. Marchan-Hernandez, H. Park, X. Bosch-Lluis, N. Rodriguez-Alvarez, I. Ramos-Perez,"Ocean Surface's Scattering Coefficient Retrieval by Delay-Doppler Map Inversion," in *IEEE Geosci. Remote Sens. Lett.*, vol. 8, no. 4, pp. 750-754, July 2011.

[5] E. Valencia, A. Camps, N. Rodriguez-Alvarez, H. Park, I. Ramos-Perez,"Using GNSS-R Imaging of the Ocean Surface for Oil Slick Detection," in *IEEE Journal of Selected Topics in Applied Earth Observations and Remote Sensing*, vol. 6, no. 1, pp. 217-223, Feb. 2013.

[6] V. U. Zavorotny, S. Gleason, E. Cardellach, A. Camps,"Tutorial on Remote Sensing Using GNSS Bistatic Radar of Opportunity," in *IEEE Geosci. Remote Sens. Magazine*, vol. 2, no. 4, pp. 8-45, Dec. 2014.

[7] M. Antoniou, M. Cherniakov, H. Ma,"Space-surface bistatic synthetic aperture radar with navigation satellite transmissions: a review," in Science China Information Sciences, vol. 58, no. 6, pp. 1-20, Jun. 2015.

[8] M. Bevis, S. Businger, T. A. Herring, C. Rocken, R. A. Anthes, R. H. Ware, "GPS meteorology: Remote sensing of atmospheric water vapor using the Global Positioning System," in *Journal of Geophysical Research: Atmospheres*, vol. 97, no. D14, pp. 15787-15801, Oct. 1992.

[9] M. Antoniou and M. Cherniakov, "GNSS-based bistatic SAR: A signal processing view," in *EURASIP Journal on Advances in Signal Processing*, no.1, pp. 1-16, Mar. 2013.

[10] C.Hu, Y. Tian, X. Yang, T. Zeng, T. Long, X. Dong, "Background Ionosphere Effects on Geosynchronous SAR Focusing: Theoretical Analysis and Verification Based on the BeiDou Navigation Satellite System (BDS)," in *IEEE Journal of Selected Topics in Applied Earth Observations and Remote Sensing*,vol. 9, no. 3, pp. 1143-1162, Mar. 2016.

[11] European space agency/European GNSS, "Galileo open service, signal in space interface control document (OS SIS ICD),"Nov. 2015.

[12] M. Antoniou, M. Cherniakov, C. Hu, "Space-surface bistatic SAR image formation algorithms," in *IEEE Trans. Geosci. Remote Sens*., vol. 47, no. 6, pp. 1827-1843, Jun. 2009.

[13] H. Ma, M. Antoniou, M. Cherniakov, "Passive GNSS-based SAR Resolution Improvement Using Joint Galileo E5 Signals," in *IEEE Geosci. Remote Sens. Lett.*, vol. 12, no. 8, pp. 1640-1644, Aug. 2015.

[14] I. Suberviola, I. Mayordomo, J. Mendizabal, "Experimental results of air target detection with a GPS forward-scattering radar," in *IEEE Geosci. Remote Sens. Lett.*, vol. 9, no.1, pp. 47-51, Jan. 2012.

[15] A. Di Simone, H. Park, D. Riccio, A. Camps, "Sea Target Detection Using Spaceborne GNSS-R Delay-Doppler Maps: Theory and Experimental Proof of Concept Using TDS-1 Data," in *IEEE Journal of Selected Topics in Applied Earth Observations and Remote Sensing*, vol. PP, no. 99, pp. 1-19, May 2017. (doi: 10.1109/JSTARS.2017.2705350)

[16] M.P. Clarizia, P. Braca, C. S. Ruf, P. Willett, "Target detection using GPS signals of opportunity," in*International Conference on Information Fusion*, Washington, DC, USA, Jul. 2015,pp. 1429-1436.

[17] A.K. Brown, “Remote sensing using bistatic GPS and a digital beam-steering receiver,” in *International Geoscience and Remote Sensing Symposium (IGARSS)*, Milan, Italy, Jul. 2015, pp. 416-419.

[18] M. Conti, F. Berizzi, M. Martorella, E. Dalle Mese, D. Petri, A. Capria, “High range resolution multichannel DVB-T passive radar,” in *IEEE Aerosp. Electron. Syst. Mag.*, vol. 27, no. 10, pp. 37-42, Oct. 2012.

[19] J.E. Palmer, H. A. Harms, S. J. Searle, L. Davis, “DVB-T passive radar signal processing,” in *IEEE Trans. Signal Process.*, vol. 61, no. 8, pp. 2116-2126,Apr. 2013.

[20] F. Colone, D. W. O'hagan, P. Lombardo, C. J. Baker, “A multistage processing algorithm for disturbance removal and target detection in passive bistatic radar,” in *IEEE Trans. Aerosp. Electron. Syst.*, vol. 45, no. 2, pp. 698-722, Apr. 2009.

[21] H.Sun, D. K. Tan, Y. Lu, “Aircraft target measurements using a GSM-based passive radar,” in *IEEE Radar Conference*, Rome, Italy, 2008, pp. 1-6.

[22] P. Marques, A. Ferreira, F. Fortes, P. Sampaio, H. Rebelo, L. Reis, “A pedagogical passive RADAR using DVB-S signals,” in *International Asia-Pacific Conference on Synthetic Aperture Radar (APSAR)*, Seoul, Korea, 2011, pp. 1-4.

[23] D. Cristallini, M. Caruso, P. Falcone, D. Langellotti, C. Bongioanni, F. Colone, S. Scafe, P. Lombardo, “Space-based passive radar enabled by the new generation of geostationary broadcast satellites,” in*IEEE Aerospace Conference*, Big Sky, MT, 2010, pp.1-11.

[24] M. Golabi, A. Sheikhi, M. Biguesh,“A new approach for sea target detection in satellite based passive radar,” in*Iranian Conference on Electrical Engineering (ICEE)*, Mashhad, Iran, 2013, pp. 1-5.

[25] F. Santi, M. Antoniou, D. Pastina, “Point spread function analysis for GNSS-based multistatic SAR,” in *IEEE Geosci. Remote Sens. Lett.*, vol. 12, no. 2, pp. 304-308, Feb. 2015.

[26] F. Santi, M. Bucciarelli, D. Pastina, M. Antoniou, M. Cherniakov, “Spatial resolution improvement in GNSS-based SAR using multistatic acquisitions and feature extraction,” in *IEEE Trans. Geosci. Remote Sens.*, vol. 54, no. 10, pp. 6217-6231, Oct. 2016.

[27] X. He, T. Zeng, M. Cherniakov, “Signal detectability in SS-BSAR with GNSS non-cooperative transmitter,” in *IEE Proceedings Radar, Sonar and Navigation*, vol. 152, no. 3, pp. 124-132, Jun. 2005.

[28] S. Chiu and C. Livingstone, “A comparison of displaced phase centre antenna and along-track interferometry techniques for RADARSAT-2 ground moving target indication,” in *Canadian Journal of Remote Sensing*, vol. 31, no.1, pp. 37-51, Jun. 2014.

[29] J.H. Ender, C. H. Gierull, D. Cerutti-Maori, “Improved space-based moving target indication via alternate transmission and receiver switching,” in *IEEE Trans. Geosci. Remote Sens.*, vol. 46, no. 12, pp. 3960-3974, Dec. 2008.

[30] K.D. Ward, S. Watts, R. J. Tough, “Sea clutter: scattering, the K distribution and radar performance,” IET, London, U.K.,2006.

[31] L. Daniel, M. Gashinova, M. Cherniakov, “Maritime target cross section estimation for an ultra-wideband forward scatter radar network,” in *European Radar Conference (EuRAD)*, Amsterdam, Netherlands, 2008, pp. 1-4.

[32] H. Griffiths, W. A. Al-Ashwal, K. D. Ward, R. J. A. Tough, C. J. Baker, K. Woodbridge, “Measurement and modelling of bistatic radar sea clutter,” in *IET Radar, Sonar and Navigation*, vol. 4, no. 2, pp. 280-292, Apr. 2010.

[33] D. Pastina and F. Turin, “Exploitation of the COSMO-SkyMed SAR System for GMTI Applications,” in *IEEE Journal of Selected Topics in Applied Earth Observations and Remote Sensing*, vol. 8, no. 3, pp. 966-979, Mar. 2015.